Experimental Investigation of the Combustion Properties of an Average Thermal Runaway Gas Mixture from Li-Ion Batteries

Olivier Mathieu*, Claire M. Grégoire, Mattias A. Turner, Darryl J. Mohr, Sulaiman A. Alturaifi, James C. Thomas, and Eric L. Petersen

J. Mike Walker '66 Department of Mechanical Engineering, Texas A&M University, College Station, 77845, Texas, USA

Abstract: To assess the fire hazard associated with venting gases coming from a lithium-ion battery during a thermal runaway, a mixture representative of such venting gas was determined by averaging forty gas compositions presented in the literature. The final mixture is composed of C₃H₈, C₂H₆, C₂H₄, CH₄, H₂, CO, and CO₂. The combustion properties of this mixture were determined using various combustion devices: shock tubes for ignition delay time measurements in air and for H₂O time histories in very dilute mixtures (99% Ar), as well as a closed bomb to measure the laminar flame speeds. Experiments were performed at around atmospheric pressure and for several equivalence ratios in all cases. Several detailed kinetics models from the literature were assessed against the data generated with this very complex mixture, and it was found that modern detailed kinetics mechanisms were capable of appropriately predicting the combustion properties of thermal runaway gases from a battery in most cases, with the NUIGMech 1.1 model being the most accurate. A numerical analysis was conducted with the two most modern models to explain the results and highlight the most important reactions.

Key words: Battery thermal runaway gases, shock tubes, laminar flame speed, detailed kinetics models

1. Introduction

Thanks to their high energy density and advantageous properties such as a lack of memory effect and a low self-discharge, lithium-ion batteries (LIB) are globally used to power the ever-growing number of mobile devices and will play a significant role in the transportation industry for years to come. In a LIB, lithium salt ions move from one electrode to the other, via an electrolyte and through a separator, during the charge/discharge cycles. The LIB electrolyte is essentially composed of a mixture of linear (dimethyl-carbonate, diethyl-carbonate, ethyl-methyl-carbonate) and cyclic (ethylene carbonate, and propylene carbonate) carbonates and is very flammable [1].

Because of the high flammability of the electrolyte, any flaw in the design or the fabrication process of the LIB leads to serious fire hazards during its usage. Examples of fire incidents involving LIBs with phones, laptops, cargo planes, and cars are frequently reported by news outlets and in the scientific literature [2,3]. The reason behind a LIB fire is always an internal short circuit and three main reasons lead to it: mechanical abuse, electrical abuse, and thermal abuse. Note that these abuses can be linked; a mechanical abuse can lead to an electrical abuse, which will then lead to a thermal abuse

^{*}Corresponding author: olivier.mathieu@tamu.edu

(inducing a thermal runaway and, potentially, fire and explosion) [3]. A fire incident by mechanical abuse is of particular concern due to the imminent proliferation of electric vehicles (EV) on the roads.

In case of a severe collision involving an EV, the battery can be crushed or penetrated, which can lead to a short circuit (electrical abuse) and eventually to thermal abuse and thermal runaway when the electrolyte reacts due to the heat [1]. As the electrolyte reacts in the battery cell (a pyrolysis process, essentially), flammable gases are created which can lead to a fire if the hot, flammable gases vent to the air. Thermal runaway gases (TRG) from Li-ion batteries have been characterized in many studies [4], but their combustion properties have never been investigated at the fundamental combustion level. One of the reasons behind that is due to the fact that the TRG composition varies widely with a large number of parameters such as the electrolyte composition, the nature of the electrode [5-7] the state of charge of the battery [5,6,8], the failure environment (air, N₂, vacuum...), the aging of the battery etc. [9]. A review and summary of the literature on TRG compositions from various types of batteries, electrodes, electrolyte composition, state of charge etc. is provided in Baird et al. [4].

A key takeaway from the Baird et al. review is that despite the large number of factors influencing the TRG composition, the detected species are very similar between studies. However, it is worth mentioning that the specific concentrations of these species can vary greatly: CH₄ varies between 73% vol. [10] and 0.12% vol. [9], H₂ between 0% vol. [9] and 35.68% vol. [11], etc. In the present study, we assembled the detailed composition of the vent gases from the studies listed in [4] and in [9], and a total of forty different compositions were identified. An average mixture was determined from these forty TRG compositions, and the procedure for determining the average composition is detailed below. The final mixture is composed of seven components and is defined in Table 1.

Table 1: Li-ion battery thermal runaway gas mixture determined and used during this study.

Fuel	C_3H_8	C_2H_6	C_2H_4	CH ₄	H_2	CO	CO_2
Mole fraction	0.007	0.019	0.027	0.119	0.144	0.168	0.516

As one can see, all the fuels listed in Table 1 have been studied extensively individually. However, to the best of our knowledge, such a complex mixture of these gases has never been investigated before. A notable absence from the list is H₂O. Given the high oxygen content in the structure of the carbonates forming the electrolyte, one could reasonably expect to see water being formed as pyrolysis product. Especially since a large fraction of CO₂ (final combustion product) is reached. The reason why water is not reported could be because it was not among the species that were looked for in the gas analysis (water not being a toxic, flammable, or a pollutant). Also, a large fraction of water could have condensed prior to the gas sampling stage. Finally, it is also worth mentioning that water was formed in much smaller concentration (and necessitated much higher temperatures to form) than CO in the study of Atherley et al. [12] with dimethyl-carbonate pyrolysis. Hence, there is the possibility that water is also formed at very small concentrations only in the conditions of the LIB thermal runaway tests reported in the literature.

Since many parameters influence the TRG composition and since the TRG composition varies widely from one study to the next, it can be concluded that the average mixture defined herein is, in a way, not representative of any real TRG composition. On the other hand, studying specific mixtures that are representative of specific batteries and conditions would lead to an excessively large experimental matrix. Thus, the unique complexity of the average TRG mixture determined herein essentially served as a target to assess the performance of detailed kinetics mechanisms from the

literature. In the end, it is reasonable to assume that the model(s) capable of predicting accurately all the data generated in the present study will also be able to reasonably predict the combustion properties of any other TRG mixture with a similar level of accuracy.

Finally, it is worth mentioning that most syngas-type mixtures studied so far in the literature are much less complex, typically limited to all or part of the following components: CO, CO₂, H₂, CH₄ and N₂ [13-22], with some other impurities in a very small number of studies [23-25]. The study of each of these typical syngas mixtures was also conducted in a limited set of conditions and experimental devices. Thus, the additional complexity of the mixture defined in Table 1 and the fact that the combustion properties of this mixture were studied experimentally through global kinetics data measurements with fuel/air mixtures (ignition delay time in a shock tube, laminar flame speed in a closed vessel) and via more fundamental experiments (H₂O laser absorption spectroscopy in dilute conditions) provide great validation targets for future model development. The results should also be beneficial to the development of most models for a broader range of combustion applications, as the CO-C3 base is common to the combustion chemistry of all hydrocarbon fuels typically used in modern combustion devices (from natural gas to diesel fuel).

First, this paper briefly describes the experimental devices used to generate the data. These data are then presented and compared to computed results from detailed kinetics models from the literature. Lastly, a numerical analysis of the results is provided using the two best performing models.

2. Experimental procedure

Several types of experiments were performed during this study to assess detailed kinetics models. Global kinetics data such as ignition delay times and laminar flame speeds were measured in a shock tube and closed vessel, respectively. These measurements allow for validation of the overall reactivity of the models, with the flame speed being typically sensitive to chain carrier and radical propagation reactions, and ignition delay time being more sensitive to reactions leading to the creation of the first radicals. The laminar flame speed measurements also involve transport properties as an additional constraint to the model. Lastly, a second shock tube was used to measure water profiles via spectroscopic measurements using a laser. This type of measurement typically involves a lower number of reactions than for the ignition delay time, and the high level of dilution used also greatly limits the effect of the exothermicity involved during the combustion. As a result, this type of measurement exacerbates the importance of the rate coefficient selected within the models, at least with regards to water formation. The combination of all these types of measurements, along with the complexity of the mixture, are great targets for model validation.

2.1 Determination of the average TRG mixture composition

As mentioned in the Introduction, the TRG mixture studied herein was defined by averaging the composition of forty detailed TRG mixture compositions from the literature using the studies from Baird et al. [4] and Spray et al. [9]. As many different components were identified in these studies, a few assumptions were made to keep the final mixture practical: the O₂ and N₂ concentration were disregarded, as they most likely essentially come from air, and not all failure tests used air as an environment; no vaporized battery electrolytes were taken into account as only one study detected them [26] and their combustion properties are not well-known (some linear carbonates) or not known at all (cyclic carbonates), so they need to be studied separately at this stage. Finally, the components with too low of an average concentration (for example, C₂H₂ and C₃H₆ would have accounted for

0.2% and 0.03% of the averaged fuel mixture, respectively), and for which preliminary computations did not show any appreciable difference in the combustion properties of the final TRG mixture, were excluded.

As stated in the introduction, several parameters influence the composition of the TRG mixture (electrolyte and electrode compositions, state of charge, aging, ramp of temperatures applied to the cell during the thermal runaway tests if a thermal failure is used, type of battery pack (pouch cells, prismatic cells, cylindrical cells), etc.) and even consecutive tests with similar battery cells can experience variations in the TRG composition [9]. The approach followed by the authors, while not specific to a type of battery and conditions, allows for estimation of the combustion properties of this type of flammable gas mixture without having to study an extremely large experimental matrix. However, to provide a better understanding to the reader, more details about the TRG compositions used to defined the average mixture are provided as follows: the TRG compositions are coming from battery cells that use various cathode compositions such as LCO (Lithium Cobalt Oxide) [10,27], LFP (Lithium FerroPhosphate) [6,11,26,28], NCA (Nickel Cobalt Aluminum) [6,7,29,30], LMO (Lithium Magnesium Oxide) [8], or unspecified composition [9]. The state of charge (SOC) of the battery cells also varied widely amongst these studies: from 0% SOC [6,10,11] to 100 % [5-9,28-30] or higher [6,8,26-28], with various increments between 0 and 100% SOC for some studies [6,8]. Several gases [6,8,9] (or vacuum [10]) and volumes [9] were used for the test environment as well. Finally the type of failure test was also different amongst the studies used for the average mixture determination, with some cycled Overcharged/Overdischarged [10], overcharged [26-28], overdischarged [11], and various types of thermal abuse [6-9, 29,30].

2.2 Ignition delay time measurements

Ignition delay time measurements of the TRG mixture were performed in a single-diaphragm (polycarbonate, 0.25-mm thickness), stainless-steel shock tube (15.24-cm i.d., 4.72-m long and 7.62cm i.d., 2.46-m long for the driven and driver sections, respectively). Five PCB-113B22 piezoelectric pressure transducers were used to measure the velocity of the incident shock wave, which was extrapolated to the endwall to determine post reflected-shock conditions. Using this method, the uncertainty in the temperature behind reflected shock waves (T₅) is maintained within 15 K [31]. Test pressure was monitored by one Kistler 603-B1 transducer located at the sidewall (16 mm from the endwall), and one PCB-113B22 transducer at the endwall. At both locations, OH* signals were recorded using an interference filter at 307 ± 10 nm. The test section was evacuated to 2×10^{-5} Torr or less using a roughing pump and a turbomolecular pump before each experiment. More details on the shock tube are available in Aul et al. [32]. The ignition delay time was measured using the time between the endwall pressure signal (to determine time zero) and the time where the tangent of the maximum slope of the OH* signal intersects with the baseline, Fig. 1. The uncertainty in these measurements is estimated to be about 15%. The post-reflected-shock pressure rise, dP/dt, is around 3%/ms in this study. Since the measured ignition delay times are below 1.5 ms, the effect of this non-ideal effect on the ignition delay time can be neglected. Note that ignition delay times measured using the pressure signal or the sidewall OH* signal (still using the endwall pressure signal to determine time zero) are almost identical to the ignition delay time measured using the endwall OH* presented herein, indicating that the ignitions were homogeneous [33,34].

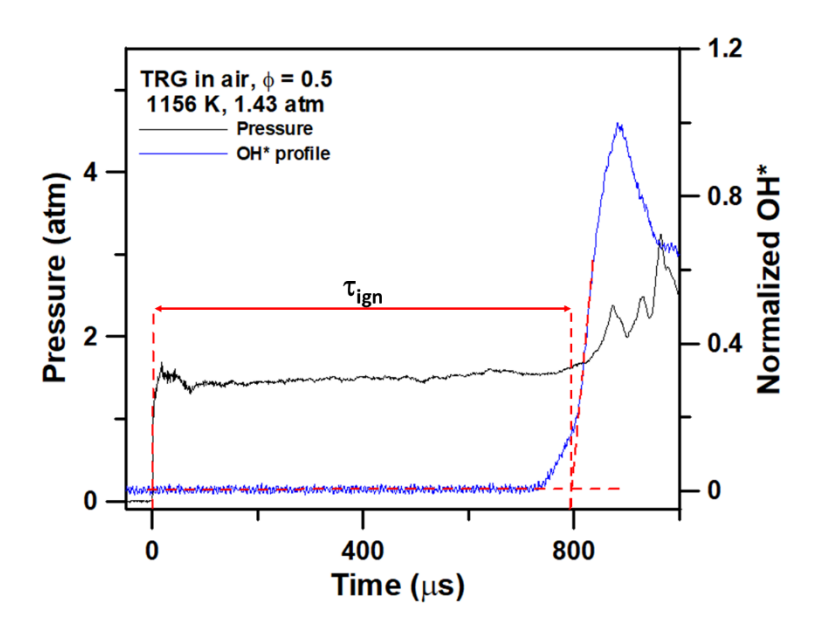


Figure 1: Determination method for the ignition delay time.

2.3 Water time-history measurements

The water measurements were taken in another single-diaphragm shock tube, also made of stainless steel. The dimensions of the laser-diagnostic shock tube are a 7.62-cm inner diameter and 3.25-m-long driver section, and a 16.2-cm inner diameter and 7.88-m-long driven section. Similar to the shock tube used for the ignition delay time measurements, the incident shock-wave velocity was obtained using the signals of piezoelectric pressure transducers located along the driven section with a well-known spacing between them. The temperature and pressure behind the reflected shock wave, T₅ and P₅, were calculated using the 1-D normal shock equations. The diaphragm thickness (0.25 mm) and material were the same as for the ignition delay time measurements. The driven section was vacuumed down to 2×10^{-5} torr or less before each run using a turbomolecular pump.

A quantum cascade laser (QCL) manufactured by Alpes Lasers was used to perform the H₂O time-history measurements. The QCL produced narrow bandwidth (~1.5 MHz) light in the midinfrared region around 7.4 μm. This wavelength corresponds to the ν₂ fundamental band of H₂O and is tunable over a frequency range of 1346–1354 cm⁻¹. The laser was positioned to access the 13_{0,13}←13_{1,12} transition at 1348.812 cm⁻¹; a wavelength that was continuously monitored via an interferometric wavemeter (Bristol instruments 671). The generated light from the QCL was split into two legs via a ZnSe plate beamsplitter representing an incident (I₀) and transmitted (I_t) intensities. The intensities from I₀ and I_t were monitored using two thermoelectrically cooled HgCdTe photovoltaic detectors (Vigo system) each with a bandwidth of 300 kHz. After the beamsplitter, I₀ passed through a few optics and then was terminated at one of the detectors to establish a reference intensity, while I_t passed through the shock tube before terminating on the other detector. The signals of I₀ and I_t were collected using a differential preamplifier to implement the common-mode rejection scheme. The two detectors were fitted with narrow bandwidth spectral filters centered at 7390 nm with a full width half maximum of 105 nm, which allowed only the laser light to pass and eliminated emission from other frequencies. This emission elimination was confirmed by repeating shock-tube

experiments while blocking the light from the laser, and no signal was observed by the detectors. A schematic of the laser diagnostic setup is presented in Fig. 2.

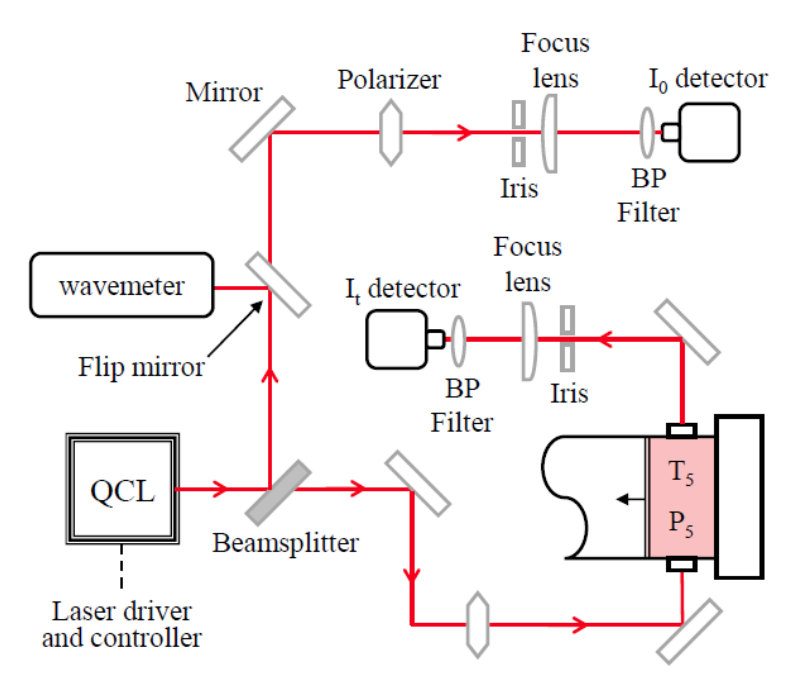


Figure 2: Schematic of the H₂O laser absorption setup.

To reduce the H₂O mole fraction from the I₀ and I_t signals, the following Beer-Lambert relation was invoked:

$$\frac{I_t}{I_0} = \exp[-k_v X_{abs} PL] \tag{1}$$

were X_{abs} is the mole fraction of the absorbing species (i.e. H_2O mole fraction), P is the mixture pressure (atm), L is the path length (cm), and k_v is the spectral absorption coefficient (cm⁻¹atm⁻¹). Separate shock-tube experiments were conducted to characterize k_v over a wide range of temperature and around atmospheric pressure. This characterization was carried out by producing a known amount of H₂O from the high-temperature reactivity of 0.009 H₂ + 0.001 O₂ in 0.99 Ar. These experiments produce an equilibrium value of 2000 ppm H₂O which was used as an input in the Beer-Lambert law, in conjunction with the measured I_0 and I_t intensities to deduce a k_v value. This H_2O equilibrium value was confirmed from the prediction of a well-developed H₂/O₂ kinetics model [35] and several prior experiments [36,37] of the same mixture. The deduced k_v values are presented in Fig. 3 along with the best fit of the data which yielded the temperature dependency relation of the absorption coefficient; this relation was subsequently utilized to calculate k_v for the present H₂O time-history experiments. During the experiments, the temperature increased from the calculated T₅ condition due to the exothermicity of the reactive mixture. This temperature change was accounted for by utilizing a time-varying k_{ν} value corresponding the temperature change per the model of Baigmohammadi et al. (NUIGMech 1.1) [38]. The temperature change was limited to ~50-60 K which led to a minor change in the final H₂O mole fraction (typically ~ 4-7%). Further detailed on the procedures utilized in processing the laser absorption signals to deduce the H₂O mole fraction can be found in Alturaifi et al. [39].

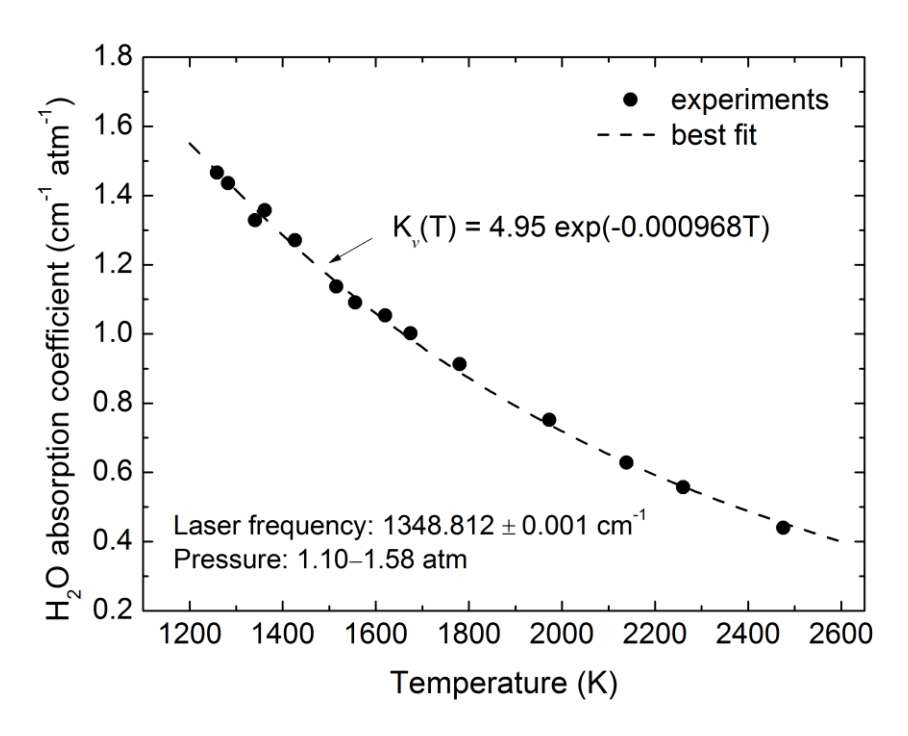


Figure 3: Spectral absorption coefficient of 2000 ppm H_2O in Ar. Dashed line presents the best fit, which was used to calculate k_v at T_5 conditions.

2.4 Laminar flame speed measurements

Spherically expanding flame experiments were conducted using a cylindrical chamber with approximately 34 L of internal volume. The chamber is equipped with opposed 12.7-cm diameter windows, providing optical access to a schlieren diagnostic. More information on the explosion chamber is given by Morones et al. [40]. A flame-front-tracking routine was developed in-house to extract flame radii from the schlieren images using contrast adjustment and Canny edge detection. The rate of change of the flame radius dr/dt is determined from the time history of the flame radius. The propagation speed of the flame relative to the burned gas $S_b = dr/dt$ was extrapolated to its unstretched value S_b^0 using NM I (Eq. 2), which is a nonlinear relationship between the burned flame speed and the stretch rate of the flame described originally by Markstein [41], investigated by Frankel and Sivashinsky [42], and analyzed in detail by Chen [43]. For spherically expanding flames with positive or near-zero Markstein lengths, NM I is highly accurate [43]. To arrive at the unstretched, unburned flame speed S_L^0 , continuity is applied in Eq. 3, where S_b^0 is multiplied by the ratio of the densities of the burned and unburned gases $\sigma = \rho_b/\rho_u$.

$$S_b = S_b^0 - S_b^0 L_{M,b} \frac{2}{r} \tag{2}$$

$$S_L^0 = \sigma S_h^0 \tag{3}$$

In Eq. 2, $L_{M,b}$ refers to the burned-gas Markstein length, and r refers to the radius of the flame. The mixture densities were calculated using AramcoMech 1.3 [44] and the equilibrium chemistry routine in Chemkin-Pro. More information on this analysis process, including a detailed breakdown of uncertainties, are given by Sikes et al. [45].

To account for the small but measurable differences in initial (room) temperature between experiments, a slight temperature correction is employed. This adjustment allows for direct comparison of the experimental data and the models at the standard temperature of 298.15 K. The temperature correction takes the form of Eq. 4, which can be found in Lowry et al. [46] and Sikes et al. [45].

$$S_{L,298}^{0} = S_{L,T_i}^{0} \left(\frac{298.15}{T_i}\right)^{\alpha} \tag{4}$$

The initial temperature of the mixture is represented by T_i . The fit constant α describes the temperature dependence of the flame speed of the mixture and is found by running a kinetics model (or actual laboratory experiments) over a range of initial temperatures. This process necessitates a suitably accurate model (in this case, AramcoMech 1.3) that captures the temperature dependence of the mixture [45]. Values for α for this study are presented in Table 2.

Table 2: Temperature dependence exponents for this study (Eq. 4).

ф	α
0.7	2.0422
0.8	1.9004
0.9	1.8194
1.0	1.7820
1.1	1.7831
1.2	1.8370
1.3	1.9782

Uncertainty in a spherically expanding laminar flame speed measurement is typically 1 to 5% and is due mostly (\sim 77%) to repeatability of the experiment and analysis procedure. Mixture composition, initial temperature, and initial pressure are responsible for approximately 14%, 8%, and 1% of total uncertainty, respectively. These values are based on gas purity and equipment accuracy in the pressure (\pm 0.05 Torr) and temperature (\pm 2 K). See Sikes et al. [45] for more information.

2.5 Mixture preparation

For all three kinds of experimental setups employed herein, the test mixtures were prepared manometrically in stainless-steel mixing tanks. The gas purities were the following: H₂, Air (premixed, certified 21% O₂, 79% N₂), and Ar are from Praxair, with 99.999% purity. The other components and purities are: CH₄ (Praxair, 99.97%), C₂H₄ (Praxair, 99.995 %), C₂H₆, (Acetylene Oxygen Company, 99.5%), C₃H₈ (Praxair, 99.5%), CO (Praxair, 99.99%), and CO₂ (Praxair, 99.99%).

For the shock tubes, the mixtures were allowed to mix overnight. The fuels for the mixtures used for the ignition delay time measurements were introduced using a 0.00-100.00 torr gage (MKS) and a 0.0-1000.0 torr gage for O₂ and CO₂ (MKS), both with an accuracy of 0.5% on the reading (N₂ was introduced using a 0.00-200.00 PSI gage). The dilute mixture for the water measurements used a 0.0000-10.0000 torr gage (MKS) for the C2-C3 hydrocarbons, whereas a 0.0-1000.0 gage (MKS) was used for CH₄, H₂, CO₂ and O₂, both with an accuracy of 0.5% on the reading (Ar being added with a 0.0-200.0 psi gage). For the laminar flame speed experiments, a large batch of the fuel mixture only (mixture in Table 1) was prepared and kept above atmospheric pressure. All components of the fuel mixture except CO₂ were introduced using a 0.0-1000.0 torr gage (MKS) with an accuracy of 0.5% on the reading. CO₂ was added using a 0.00-100.00 psi gage. The fuel mixture defined in Table 1 was then introduced into the vessel before adding in air, to the desired equivalence ratio and to atmospheric pressure. The fuel and air mixture was allowed to rest and mix for 30 minutes in the vessel before being ignited. Mixtures studied herein are listed in Table 3 (the fuel mixture for the flame speed experiments is defined in Table 1).

Table 3: Composition of the mixtures used during the shock-tube experiments.

	TRG mixture composition (mole fraction)									
	Shock tube ignition delay time									
ф	H_2	CH ₄	C_2H_4	C_2H_6	C_3H_8	CO	CO_2	O_2	N_2	Ar
0.5	0.02219	0.01834	0.00416	0.00293	0.00108	0.02589	0.0795	0.1776	0.66831	0.00
1.0	0.03845	0.03177	0.00721	0.00507	0.00187	0.04486	0.13778	0.1539	0.57909	0.00
2.0	0.06069	0.05016	0.01138	0.00801	0.00295	0.07081	0.21748	0.1215	0.45702	0.00
	Shock tube H ₂ O absorption									
0.5	0.00067	0.00055	0.00013	0.00009	0.00003	0.00078	0.0024	0.00535	0.00	0.99
1.0	0.00091	0.00076	0.00017	0.00012	0.00004	0.00107	0.00327	0.00366	0.00	0.99
2.0	0.00112	0.00092	0.00021	0.00015	0.00005	0.0013	0.00401	0.00224	0.00	0.99

3. Detailed chemical kinetics models

As mentioned above, the complex mixture studied herein is a great way to assess the accuracy of detailed chemical kinetics mechanisms available in the literature. The following models were used for comparison with the data and assessment: GRI3.0 [47], JetSurfII [48], AramcoMech 1.3 [44], CRECK2003 [49], and NUIGMech 1.1 [38]. The number of species and reactions in each model are listed in Table 4. These models were selected as they represent the historical "gold standards" in terms of validation and rate coefficient selection at their time. The differences in size amongst these models (number of species and reactions) are due to differences in the completeness of the reaction schemes (no low-temperature chemistry for the hydrocarbons in GRI3.0, for example) and the size of the molecules considered within each model (up to C₃ for GRI3.0 and CRECK2003 for example, and up to C₈ for NUIGMech 1.1).

Table 4: Detailed kinetics mechanisms used during this study.

Mechanism	Year	Number of species	Number of reactions
GRI3.0 [47]	1999	53	325
JetSurfII [48]	2010	348	2163
AramcoMech 1.3 [44]	2013	253	1542

CRECK2003 [49]	2020	114	1999
NUIGMech 1.1 [38]	2020	2746	11275

4. Experimental results and comparison with models

4.1 Ignition delay time

The ignition delay time (τ_{ign}) results are visible in Fig. 4, and the data are available as supplementary material. The comparison between the equivalence ratios (ϕ) investigated, Fig. 4, shows a large effect of the equivalence ratio on the ignition delay time. Increasing the equivalence ratio from 0.5 to 1.0 increases the ignition delay time from between a factor of about 2 (high temperature) and 1.5 (low temperature). Similar factors are observed when increasing the equivalence ratio from 1.0 to 2.0.

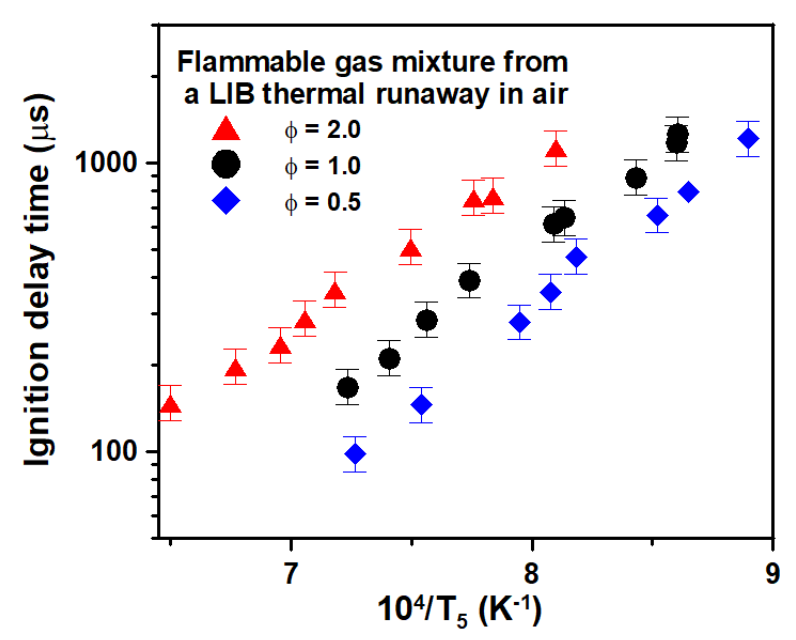


Figure 4: Ignition delay times of an average mixture of thermal runaway gases from a Li-ion battery (Table 1) at various equivalence ratios

The comparison between the data in Fig. 4 and the models is visible in Fig. 5. Overall, the models tend to converge on the high-temperature side, but they also tend to diverge at low temperatures. For the fuel-lean results, (Fig. 5(a)) the comparison with the models shows that the models considered in this study are relatively accurate and within or close to the experimental uncertainty above 1250 K but tend to underpredict ignition delay time by about 10-20% on the low-temperature side. Below this temperature, it is interesting to observe that the two oldest models considered herein are very close to the data (the GRI3.0 model being the closest to this set of data overall), whereas the modern mechanisms over-predict the increase of the delay as the temperature decreases by 33% (NUIG 1.1 and CRECK 2003) or higher (AramcoMech 1.3).

For the stoichiometric condition (Fig. 5(b)), the GRI3.0 mechanism is this time the least accurate and predicts ignition delay times that are too short by a factor of about 1.5-2.0 but presents an activation energy that is close to the data. The JetSurf II model is closer to the data on the colder-temperature side, and the three recent models are close to the data overall (under-estimation of the ignition delay time by about 20% on the high-temperature side, and over-estimation by about 20-25%

on the low-temperature side) but also tend to over-predict the activation energy. For the fuel-rich data (Fig. 5(c)), the prediction difference amongst the models is larger, and the NUIG 1.1 model is the only one that is relatively accurate in predicting the data (within 20-25%). The other models present an over-reactivity (too short of an ignition delay time), especially for the JetSurf II and GRI3.0 models with a difference of about 55% with the data. It is worth mentioning that lower temperatures (below 1000 K) would be necessary to fully validate models for battery fire conditions, but calculations with the most recent models [38,49] did not show any change in the trends seen in Fig. 5 for temperatures as low as 800-850 K, giving ignition delay times in the 3-5 seconds time-range.

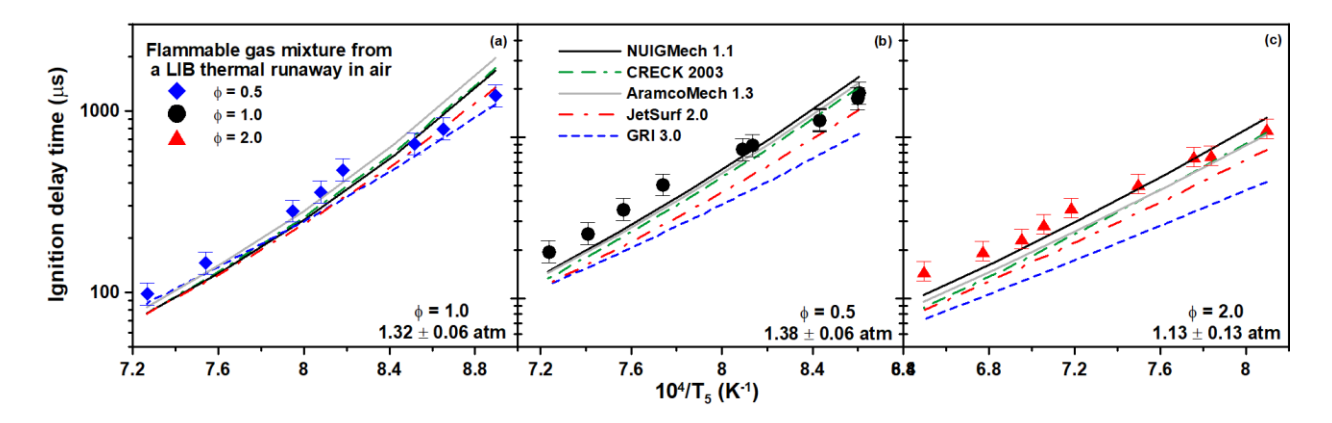


Figure 5: Ignition delay times of an average mixture of thermal runaway gases from a Li-ion battery (Table 1) at various equivalence ratios and comparison with models from the literature ((a) $\phi = 0.5$, (b) $\phi = 1.0$, (c) $\phi = 2.0$).

To provide the reader with an accurate assessment of the models' performance, the absolute error for each data point was calculated using the following equation:

$$E_i = log_{10} \frac{\tau_{ign \, model}^i}{\tau_{ign \, experiment}^i} \times 100$$
 (5)

The values obtained for each point were then averaged, and the average error of each model is reported for each equivalence ratio in Table 5.

Table 5: Error percentages on the ignition delay times of a TRG mixture predicted by the models. The averaged value on the last row correspond to the average of all individual values for all equivalence ratios.

ф	GRI 3.0	JetSurf II	AramcoMech 1.3	CRECK 2003	NUIGMech 1.1
0.5	11.2	7.5	9.3	10.0	9.8
1.0	25.5	15.5	9.0	11.3	9.0
2.0	51.5	20.2	13.1	17.8	8.5
Avg.	30.1	14.7	10.5	13.1	9.1

4.2 H₂O profiles

Representative examples for the H_2O time histories and comparison with the detailed kinetics models considered herein are visible in Fig. 6 for $\phi = 0.5$ (a-c), $\phi = 1.0$ (d-f), $\phi = 2.0$ (g-i), and the other profiles measured during this study are available as supplemental material. For all conditions investigated, the water profile is relatively similar and consists of a very slow formation of water at the beginning of the experiment, followed by a rapid and large increase in the water concentration before reaching a plateau (when the timeframe of the experiment allowed). The timing between the initial, slow formation of water and the rapid and large increase in the water profile is strongly temperature dependent-the lower the temperature, the longer the delay. An induction delay time for water has been measured for each experiment, as discussed below. Note that the spike in the water signals at around time zero does not correspond to the presence of water but is due to the rapid change in density gradient when the reflected shock wave passes into the path of the laser beam (not shown in Fig. 6 but visible in Fig. 7 as a similar peak occurring earlier for the passage of the incident shock wave). The net result of this rapid density change is temporary beam steering of the laser to a less sensitive part of the sensor, resulting in an apparent absorption signal.

Concerning the comparison with the detailed kinetics models considered, they all correctly predict the shape of the experimental profiles, although some improvements on the induction delay time are necessary in some conditions, discussed below. The rate of H₂O formation, corresponding to the large increase in the water profile, seems to be too rapid for most models, as visible in Fig. 6(h), for example. The predicted level of H₂O is very close between these models and also between the models and the data, with some minor discrepancy on the high-temperature side for the fuel-rich mixture (Fig. 6(i)).

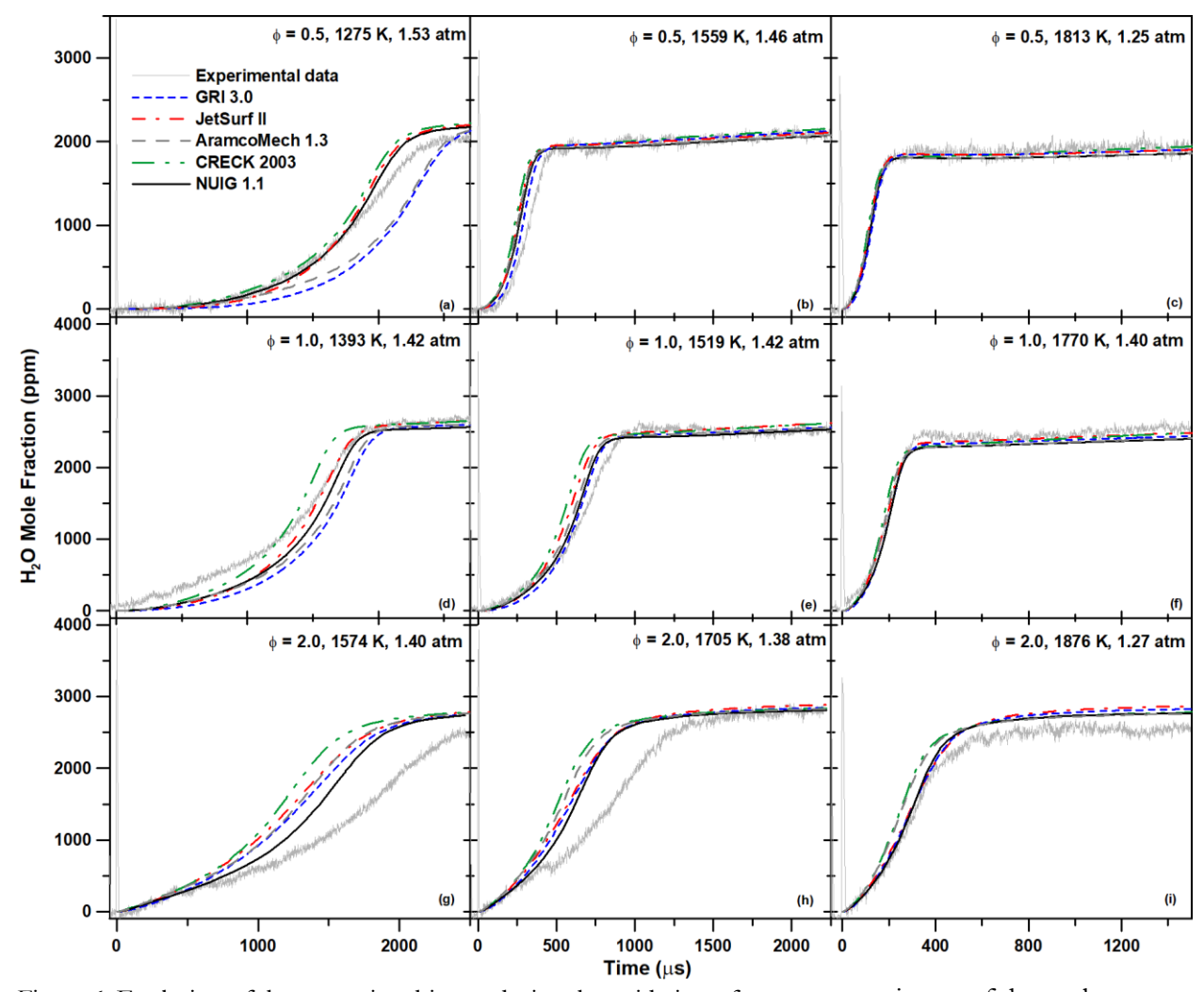


Figure 6: Evolution of the water time history during the oxidation of an average mixture of thermal runaway gases from a Li-ion battery in 99% Ar for several equivalence ratios (ϕ = 0.5 (a-c), ϕ =1.0 (d-f), ϕ =2.0 (g-i)) and temperatures.

As mentioned above, the experimental water profiles can be used to extract a H_2O induction delay time for each condition. The method is similar to the method used for the ignition delay time above, Fig. 1, and consists of extrapolating the tangent to the maximum slope of the water profile to the baseline, as visible in Fig. 7. Like for the ignition delay time above, the uncertainty in these measurements is estimated to be around 15%.

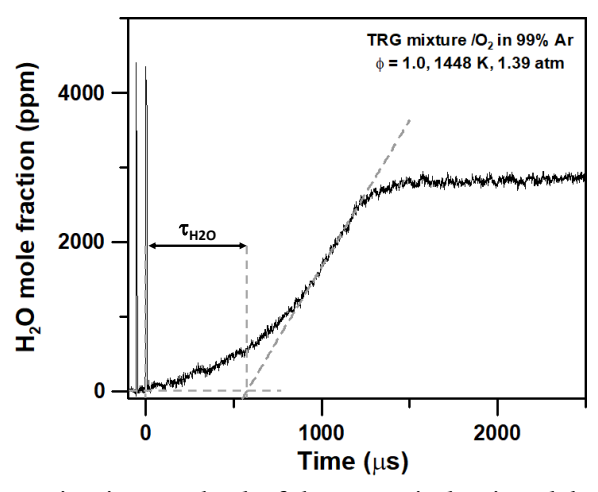


Figure 7: Determination method of the water induction delay time (τ_{H2O}).

The water induction delay time extracted from the experimental and predicted H₂O profiles are plotted versus the inverse of the temperature in Fig. 8 for each equivalence ratio (these data are available in the Supplementary Material section). As one can see, all models are in good agreement with the experimental data for the stoichiometric case, Fig. 8(b). For the lean condition, Fig. 8(a), there are some small discrepancies between the models and the data. The GRI 3.0 model predicts the water induction delay time the best, while the JetSurf II and NUIGMech 1.1 mechanisms are fairly accurate, within 25-30%. For the other models, the global activation energy, corresponding to the slope of the prediction line, is a bit too high, inducing induction delay times for water that are too short on the high-temperature side. Finally, for the fuel-rich case (Fig. 8(c)), the global activation energy is well predicted by all models, but only NUIGMech 1.1 appears to be accurately predicting the data within the uncertainties, all other models being over-reactive by 35-50% and having very similar predictions.

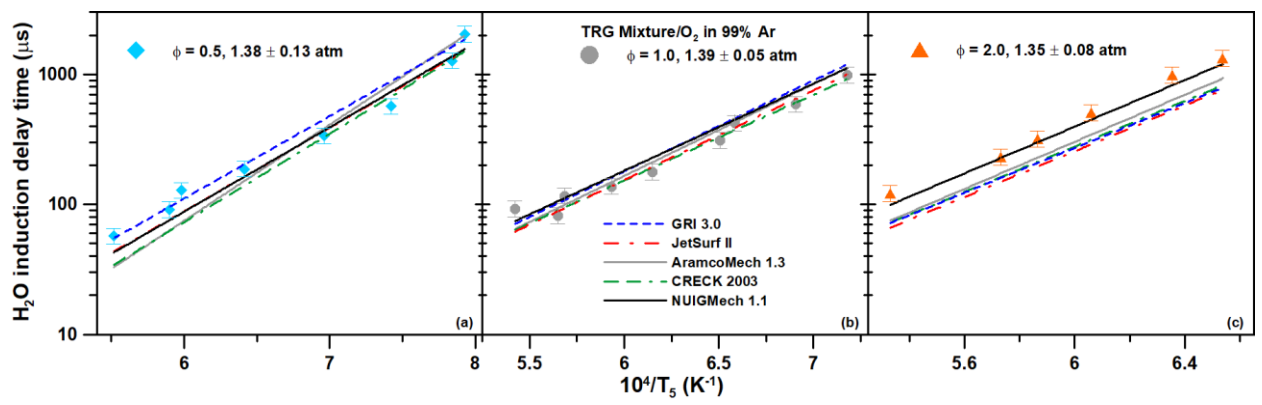


Figure 8: Experimental and predicted water induction delay time extracted from the water time-history profiles obtained during this study for $\phi = 0.5$ (a), $\phi = 1.0$ (b), and $\phi = 2.0$ (c).

Like for the ignition delay time above, the relative error of the models' prediction when compared to the data was estimated using Eq. (5). The results are visible in Table 6 and, as one can see, the NUIGMech 1.1 mechanism is the most accurate model overall, whereas the other mechanisms are globally close to each other under the conditions on the present study.

Table 6: Error percentages on the water induction delay times of a TRG mixture predicted by the models. The averaged value on the last row correspond to the average of all individual values for all equivalence ratios.

ф	GRI 3.0	JetSurf II	AramcoMech 1.3	CRECK 2003	NUIGMech 1.1
0.5	7.7	8.9	13.1	12.9	8.8
1.0	9.0	4.8	6.1	4.0	6.8
2.0	21.3	23.8	16.7	20.2	5.1
Avg.	11.8	11.2	11.3	11.3	7.0

4.3 Laminar flame speed

As can be seen in Fig. 9, the laminar flame speed of the TRG mixture presents the classical shape observed with hydrocarbons and passes by a maximum (23.25 cm/s) at an equivalence ratio of around 1.1, also like most hydrocarbons (despite the fact that H_2 or H_2 /CO mixtures have a maximum flame speed observed for much higher ϕ [13,50] and that H_2 and CO are in large proportions in the mixture studied, Table 1). The experimental data visible in Fig. 8, along with the associated Markstein lengths, are provided in the Supplementary Material section.

Concerning the models, only the CRECK and, to a lesser extent, NUIG 1.1 and AramcoMech 1.3 models are able to reproduce the data with high accuracy, within the uncertainty. The GRI3.0 model is the only one that over-predicts the data (over the entire range of equivalence ratios investigated) by about 7.5% at the peak value. The other model considered (JetSurfII) tends to under-estimate the flame speed above $\phi = 0.9$, by up to about 5%, the experimental uncertainty being estimated to be below 3% [14].

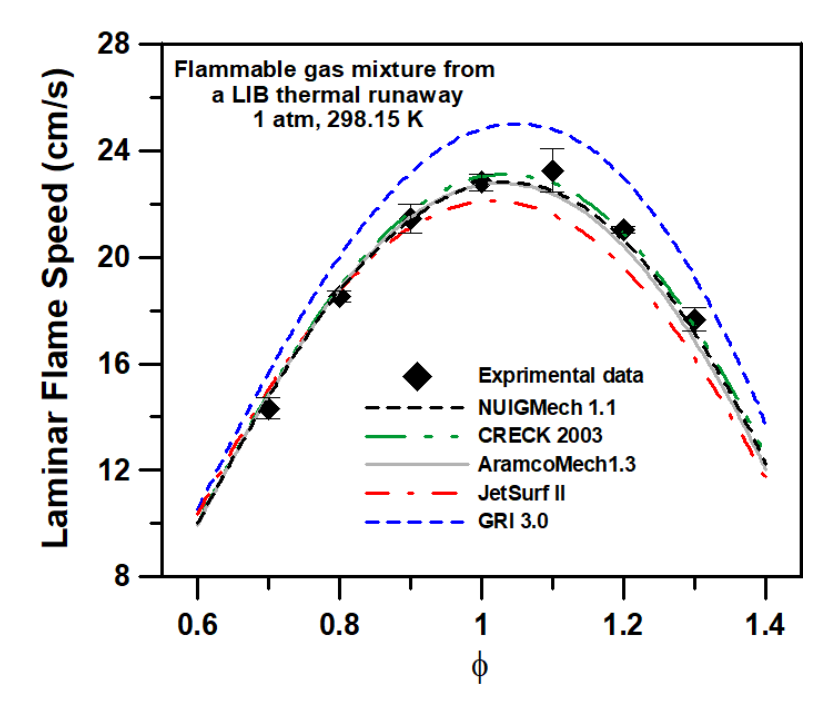


Figure 9: Laminar flame speeds of an average flammable gas mixture of the gases formed during a thermal runaway from a Li-ion battery (Table 1) in air at 1 atm and an initial temperature of 298 K.

5. Discussion

To understand and explain the results from this study, a numerical analysis was conducted with the NUIGMech 1.1 and CRECK 2003 models, as the NUIGMech 1.1 is the most accurate overall, and these two detailed kinetics mechanisms are the most recent. The good performance of these models compared to the older ones lies in the selection of the rate coefficients used (with more accurate rate coefficients being available) and to the larger set of data available to validate the models. Concerning the ignition delay time, Fig. 5, the two models considered are in good agreement with the data. A sensitivity analysis at $\phi = 1.0$, 1300 K was conducted using Chemkin, as visible in Fig. 10. As one can see, nine out of the ten most sensitive reactions are identical between the two models, their normalized sensitivity being relatively similar as well. The only different reactions between the models are also reactions with the lowest, or among the lowest, sensitivity coefficients in both cases.

In both cases, the most sensitive reaction is, by a large extent, the classical chain branching reaction R1: $O_2 + H \leftrightarrows OH + O$. The other promoting reactions are all chain propagating reactions, where one radical (or two radicals in the case of R2: $CH_3 + HO_2 \leftrightarrows CH_3O + OH$) is converted to a more reactive radical or produces a radical H that will further promote R1. Interestingly, all the inhibiting reactions common to the two models involve the not very reactive CH_3 radical, which is either produced by reaction of methane with a reactive radical ($CH_4 + OH \leftrightarrows CH_3 + H_2O$ (R3), $CH_4 + H$ $\leftrightarrows CH_3 + H_2$ (R4)) or involved into a chain terminating reaction ($CH_3 + H$ (+M) $\leftrightarrows CH_4$ (+M), R5).

As visible in Fig. 5, the predictions of the two models considered for the numerical analysis are very close for the conditions considered in Fig. 10. However, while the sensitive reactions appear to the same, it is worth mentioning that the reaction rate coefficients selected for these reactions vary between the two models: the rate coefficients for R3-R7 (R6: $H_2+OH \leftrightarrows H + H_2O$; R7: $C_2H_4 + OH \leftrightarrows C_2H_3 + H_2O$) are indeed different between the NUIGMech 1.1 and CRECK 2003 models. The choice of the reaction rate coefficient for R5 was found to have a large importance on the CO profiles obtained during CH₄ oxidation in Mathieu et al. [51]. For the most sensitive reaction, R1, the models used the same source but with some modification: R1 is about 10% faster for the CRECK model. Note that R2 and R8 (R8: $C_2H_4+H(+M) \leftrightarrows C_2H_5(+M)$) use the same parameters.

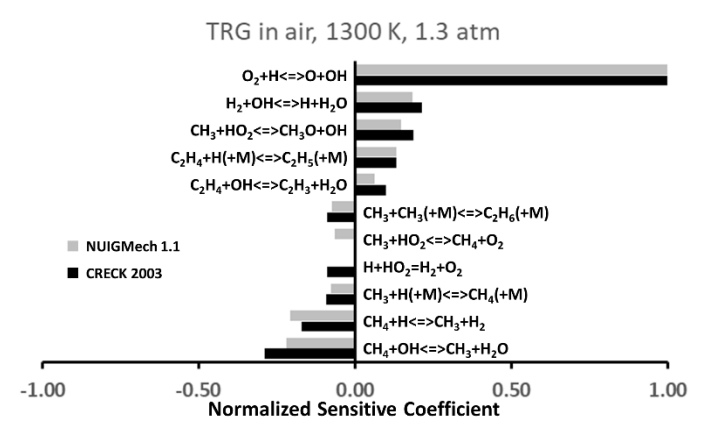


Figure 10: Sensitivity analysis on OH for the TRG mixture in air, $\phi = 1.0$, at 1300 K and 1.3 atm for the NUIGMech 1.1 and CRECK 2003 models.

Although the different reaction rate coefficient selections for these sensitive reactions does not induce large differences in the predictions for ignition delay time predictions with fuel/air mixtures, it seems that these differences matter more in dilute conditions, as can be seen in Fig. 6(g). Indeed, in fuel/air mixtures, at least in the high-temperature domain, the kinetics is driven by the large exothermicity induced by the large fuel/ O_2 concentration. In very dilute mixtures, this exothermicity is strongly mitigated and the reactivity is therefore more sensitive to differences between the reaction pathways, if any, and the reaction rate coefficients selected. Results of the sensitivity and rate of production (ROP) analyses for H_2O with the NUIGMech 1.1 and CRECK 2003 mechanisms are visible in Fig. 11, for a condition ($\phi = 2.0$, 1574 K) where a noticeable difference in reactivity is seen between the two models, and between the models and the experimental profile.

The ROP analysis shows that, for both models, the formation of water chiefly occurs via $H_2+OH \Rightarrow H + H_2O$ (R6) followed by $CH_4 + OH \Rightarrow CH_3 + H_2O$ (R3) and $C_2H_4 + OH \Rightarrow C_2H_3 + H_2O$ (R7), with R3 and R7 having a larger production for the CRECK model than for the NUIGMech 1.1 mechanism. One can also see a very small contribution of $C_2H_6 + OH \Rightarrow C_2H_5 + H_2O$ (R9), while the remaining reactions have a very small effect of the amount of water produced (with four out of six reactions being common between the models). It is interesting to note that the four main reactions behind the formation of water (R3, R6, R7, and R9) involve one of the components of the fuel mixture, and that their hierarchical contribution to the amount of water formed follows the same order as for the mole fraction of the fuel components. Note that the contribution from R6 ($H_2+OH \Rightarrow H + H_2O$) is disproportionally large compared to the relative mole fraction of H_2 with the other fuels. This large contribution from R6 is due to the H-abstraction reactions from H radicals, such as $CH_4 + H \Rightarrow CH_3 + H_2$ (R4), which produce H_2 . It is important to mention that R3, R6, R7 and R9 all have a different reaction rate coefficient between the two models, explaining the difference in reactivity seen in Fig. 11(a-b).

Other reactions moderately contributing to the formation of water and common to the two models are CH₂O + OH \leftrightarrows HCO + H₂O (R10), CH₃ + OH \leftrightarrows CH₂(S)+H₂O (R11) and CH₃ + OH \leftrightarrows CH₂ + H₂O (R12), while the reaction consuming water, H₂O+O \leftrightarrows 2OH (R13) is also predicted. Among the ten most important ROP reactions, the CRECK model predicts another H₂O consuming reaction: H₂O + CH \leftrightarrows H + CH₂O (R14) as well as the formation of water via H + OH + M \leftrightarrows H₂O + M (R15). Regarding NUIGMech 1.1, the two remaining reactions important to water formation (within the top ten) are HCOH + O₂ \leftrightarrows CO₂ + H₂O (R16) and CH₂ + OH \leftrightarrows CH + H₂O (R17).

Concerning the sensitivity analysis, Fig. 11(e-f), seven out of the top ten reactions are common to the two models. The most sensitive reaction is by far the branching (and promoting) reaction R1 ($O_2 + H \leftrightarrows OH + O$). Other promoting reactions are C_3H_8 (+M) $\leftrightarrows CH_3 + C_2H_5$ (+M) (R18), which corresponds to the thermal dissociation of C_3H_8 (important at the very beginning of the experiment), $H_2+OH \leftrightarrows H + H_2O$ (R6), and $C_2H_4 + H$ (+M) $\leftrightarrows C_2H_5$ (+M) (R8, in reverse). The reaction $O + H_2 \rightrightarrows OH + H$ (R19) has a noticeable influence for the NUIGMech 1.1 model whereas the reactions $CH_3 + O_2 \leftrightarrows CH_2O + OH$ (R20), $IC_3H_7 + H \leftrightarrows C_3H_8$ (R21, in reverse) (NUIGMech 1.1) and $HCOOH \leftrightarrows H_2O + CO$ (R22) and $HCOOH \leftrightarrows H_2 + CO_2$ (R23) (CRECK 2003) have a very small normalized sensitivity coefficient. Among the most promoting reactions, as said before, R1 and R8 have the same reaction rate coefficient (within 10% for R1) between the two models. However, R6 and R18 use different reaction parameters. The most inhibiting reactions for H_2O formation, according to both models, is $CH_4 + H \leftrightarrows CH_3 + H_2$ (R4) followed by $CH_3 + H$ (+M) $\leftrightarrows CH_4$ (+M) (R5) and $CH_3 + O$

 \leftrightarrows CH₂O + H (R24). According to the CRECK model, the reaction CH₄ + OH \leftrightarrows CH₃ + H₂O (R3) also has a relatively large inhibiting sensitivity coefficient. Amongst these inhibiting reactions, as seen above, R3-R5 have a different reaction rate coefficient selection between the two models considered, whereas these parameters are the same for R24.

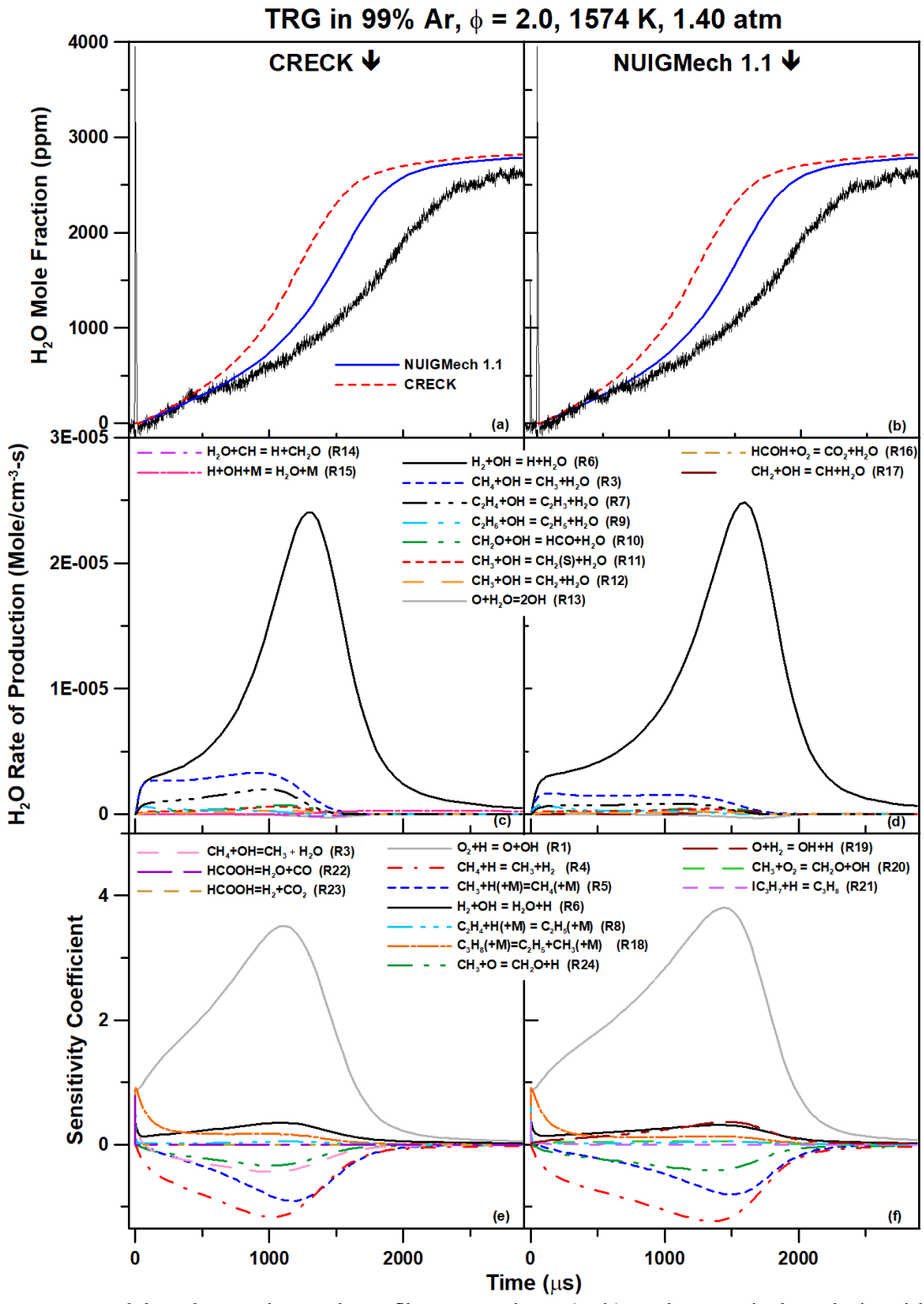


Figure 11: Model and experimental profile comparison (a, b) and numerical analysis with rate of production (c, d) and sensitivity analysis (e, f) for H_2O formation from a TRG mixture at $\phi = 2.0$, 1574 K, and 1.40 atm in 99% Ar. Left column is for the CRECK 2003 model [49], and the right column is for the NUIGMech 1.1 model [38].

Concerning the laminar flame speed, it was observed that, according to the models, the laminar flame speed correlates with the peak net heat production. An example of such a correlation is provided in Fig. 12 for the NUIGMech 1.1 mechanism. As one can see, the laminar flame speed increases in a linear fashion with the peak, net heat production, and a linear fit can be applied. Because of the shape of the laminar flame speed curve where a maximum is reached at around $\phi = 1.0$ -1.1, Fig. 9, the fuel-rich data (the equivalence ratio corresponds to the number above each point) are mixed with fuel-lean data in Fig. 12. However, it is interesting to see that the fuel-rich data are typically slightly under the line defined by the fit, whereas the fuel-lean mixtures tend to be slightly above the fit. This trend might be due to the excess of hydrocarbons in the fuel-rich flames, which undergo a series of endothermic thermal dissociation reactions.

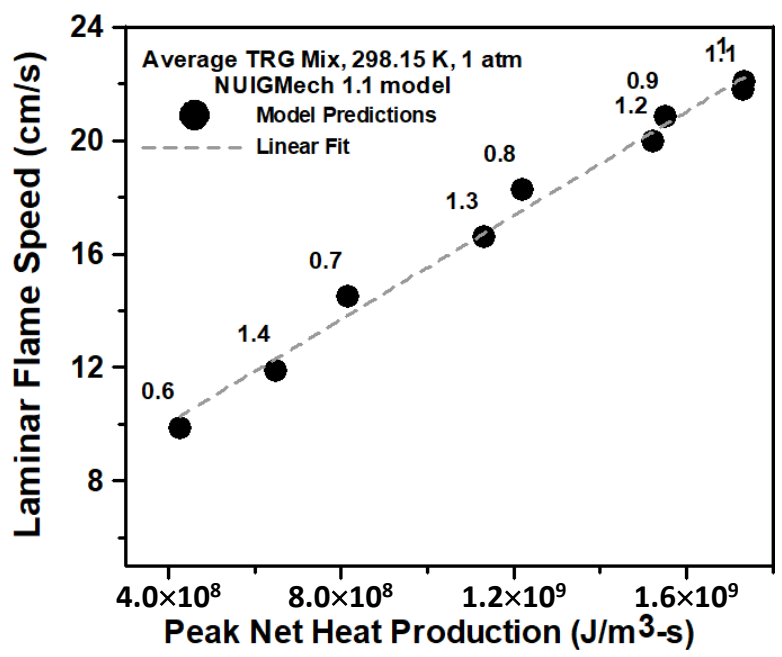


Figure 12: Evolution of the laminar flame speed as a function of the peak net heat production based on the NUIGMech 1.1 mechanism. The numbers above the point correspond to the equivalence ratios.

Since, as per Fig. 12, there is a direct correlation between the peak net heat production and the laminar flame speed, the assumption is that the reactions mainly contributing to the heat release are the ones having the largest influence on the laminar flame speed. These reactions were identified in the NUIGMech 1.1, and the results are visible in Fig. 13. These results illustrate the aforementioned differences in the importance of specific reactions for this combustion parameter compared to the shock-tube conditions. For instance, it is first interesting to mention that the reaction that has the largest heat production and should contribute to and promote the most to the flame velocity (R24: $CH_3 + O \Rightarrow CH_2O + H$) is a reaction that has a moderate but negative sensitivity coefficient with regards to water formation in the shock tube (Fig. 11). Then, the most sensitive reaction at our shock-tube conditions is the branching reaction R1: $O_2 + H \Rightarrow OH + O$, which is also a highly endothermic reaction (Fig. 13), and thus could inhibit the laminar flame speed. On the other hand, R5: $CH_3 + H$

(+M) \leftrightarrows CH₄ (+M), is a terminating reaction that has a negative sensitivity coefficient at shock-tube conditions, but this radical recombination is also highly exothermic and could promote the laminar flame speed. R6 is another reaction present at the shock-tube conditions, and this time it is interesting to see that R6 has a promoting effect in all conditions investigated herein. Other noticeable reactions for the flame speed analysis in Fig. 13 are R25-27, which are not sensitive to our shock-tube conditions. Finally, R8 (C₂H₄+H(+M) \leftrightarrows C₂H₅(+M)) has very little importance in Fig. 13, but it can be seen that R8 has a small exothermic contribution before the front flame and a more important (but still modest) endothermic contribution after, most likely due to a change in the direction of the reaction. These results illustrate the necessity of having several types of experiments to fully validate and assess the models.

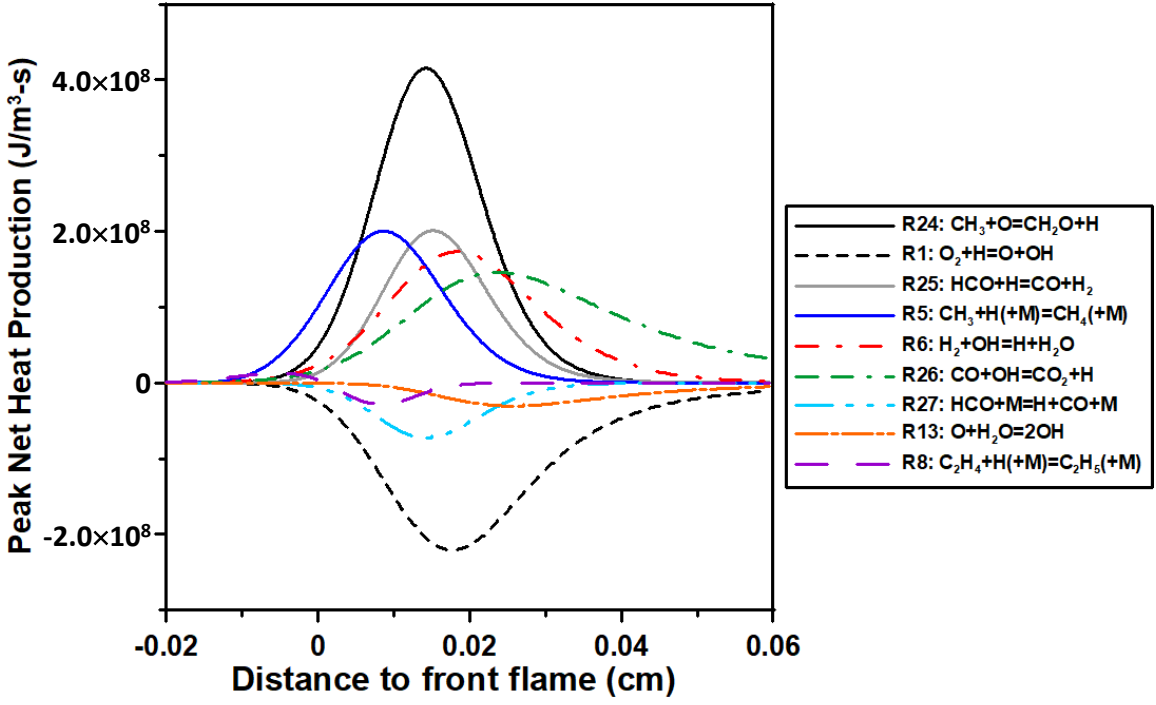


Figure 13: highest contributing reactions to the peak net heat production for the TRG mixture defined in Table 1 at $\phi = 1.0$, 298.15 K, and 1 atm.

6. Conclusions

An average mixture of vent gases from the thermal runaway of Lithium-ion batteries was determined based on forty different mixtures from the literature. The final mixture contains seven components, and the combustion of this complex mixture was investigated in shock tubes (ignition delay time, water time history by laser absorption) and closed vessel (laminar flame speed). Results were compared to detailed kinetics mechanisms from the literature. Recent detailed kinetics mechanisms can predict the data rather accurately, with the most recent one (NUIGMech 1.1) being the most accurate overall, closely followed by the ArmacoMech 1.3 and CRECK 2003 models. A numerical analysis showed that most of the sensitive reactions for the ignition delay time and the water formation were the same between the two most recent models, i.e. NUIGMech 1.1 and CRECK 2003. The ROP analysis led to the same conclusion. One can therefore conclude that both models agree regarding the reaction pathways for the oxidation of this complex fuel mixture, and that the differences

in the predictions between these two models are almost entirely due to the reaction rate coefficient selected. The complexity of the present mixture, investigated for the first time, will allow for further improvements of the base models in the future. Concerning thermal runaway mixtures from lithiumion batteries, based on the accuracy displayed by the NUIGMech 1.1 model observed herein for the average mixture, it can be concluded that this model could be used to predict the combustion properties of this type of mixture to assess the fire hazard associated with venting gases from LIB, at least at around 1 atm. However, it would be interesting to study some of the extreme mixtures used to determine the average mixture used herein in a subsequent study. For example, one of the TRG compositions in the work of Kumai et al. [10] does not contain H₂ but large concentrations of hydrocarbons (73% CH₄, 7% C₂H₆, and 7.9% C₃H₈), with only 4.1% CO (mol%), whereas one of the mixtures in the study of Golubkov et al. [6] contains 28.8% H₂ and only 6.4% CH₄ and 1.3% C₂H₄ for the hydrocarbon part, with 46.6% CO (mol%).

7. Supporting Information

Ignition delay time, H₂O induction delay times, laminar flame speeds, and Markstein lengths are available as supporting information.

8. Acknowledgments

The authors would like to thank the National Science Foundation for the financial support of this study (award # 2037795). Additional support came from the TEES Turbomachinery Laboratory and from King Fahd University of Petroleum and Minerals (KFUPM) through Saudi Arabian Cultural Mission (SACM) fellowship# 1440/10079/9 for S. Alturaifi.

9. References:

_

^[1] Guo, F., Hase, W., Ozaki, Y., Konno, Y., Inatsuki, M., Nishimura, K., Hashimoto, N., Fujita O. Experimental study on flammability limits of electrolyte solvents in lithium ion batteries using a wick combustion method. Exp. Thermal Fluid Sci., 2019, 109, 109858.

^[2] Feng, X., Ouyang, M., Liu, X., Lu, L., Xia, Y., He, X. Thermal runaway mechanism of lithium ion battery for electric vehicles: A review. Energy Storage Materials, 2018, 10, 246–267.

^[3] Wang, Q., Mao, B., Stoliarov, S. I., Sun, J. A review of lithium ion battery failure mechanisms and fire prevention strategies. Prog. Energy Combust. Sci., 2019, 73, 95–131.

^[4] Baird, A. R., Archibald, E. J., Marr, K. C., Ofodike A., Ezekoye, O. A. Explosion hazards from lithium-ion battery vent gas. J. Pow. Sources, 2020, 446, 227257.

^[5] Golubkov, A. W., Fuchs, D., Wagner, J., Wiltsche, H., Stangl, C. Fauler, G., Voitic, G., Thalera, A., Hackere, V. Thermal-runaway experiments on consumer Li-ion batteries with metal-oxide and olivin-type cathodes. RSC Adv., 2014, 4, 3633-3642.

^[6] Golubkov, A.W., Scheikl, S., Planteu, R., Voitic, G., Wiltsche, H., Stangl, C., Fauler, G., Thaler, A., Hacker, V. Thermal runaway of commercial 18650 Li-ion batteries with LFP and NCA cathodes – impact of state of charge and overcharge. RSC Adv., 2015, 5, 57171–57186.

^[7] Lammer M., Königseder, A., Hacker, V. Holistic methodology for characterisation of the thermally induced failure of commercially available 18650 lithium ion cells. RSC Adv., 2017, 7, 24425.

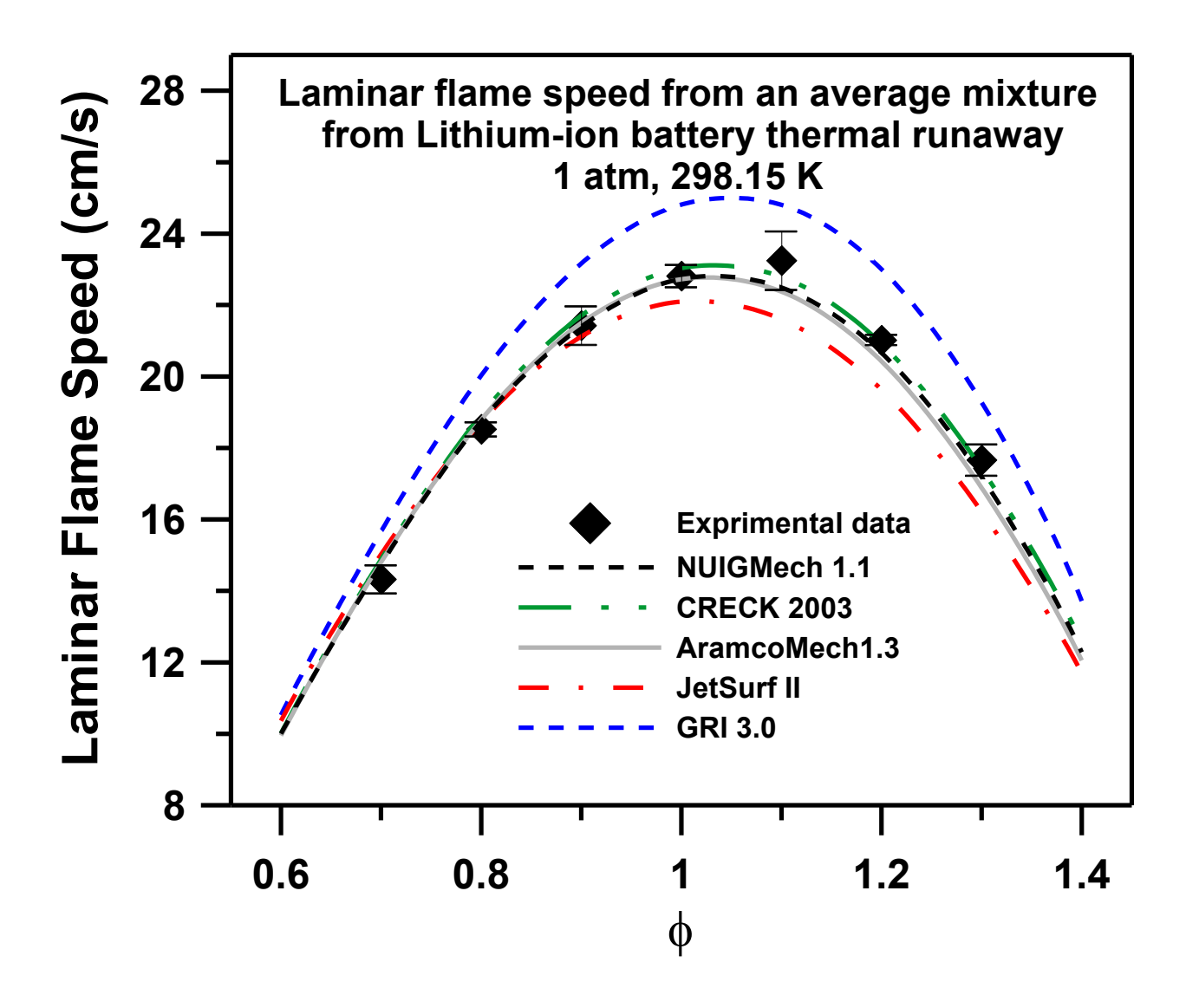
^[8] Somandepalli, V., Marr, K., Horn, Q. Quantification of combustion hazards of thermal runaway failures in lithiumion batteries, SAE Int. J. Alt. Power. 2014, 3, 98-104.

^[9] Spray R., Barry M., Vickery J., Myers T. Understanding how testing conditions affect hazard quantification in Lithium-ion battery abuse tests. NASA Aerospace Battery Workshop (Virtual), 2020. Available at (last consulted on 10/18/2021): https://www.nasa.gov/sites/default/files/atoms/files/nabw20_how_test_cond_affect_haz_quan_li-ion_batt_abuse_test_rspray.pdf.

^[10] Kumai, K., Miyashiro, H., Kobayashi, Y., Takei, K., Ishikawa, R. Gas generation mechanism due to electrolyte decomposition in commercial lithium-ion cell. J. Power Sources, 1999, 81–82, 715–719.

- [11] Zheng, Y., Qian, K., Luo, D., Li, Y., Lu, Q., Li, B., He, Y.-B., Wang, X., Li, J., Kang, F. Influence of over-discharge on the lifetime and performance of LiFePO4/graphite batteries. RSC Adv., 2016, 6, 30474–30483.
- [12] Atherley, T., de Persis, S., Chaumeix, N., Fernandes, Y., Bry, A., Comandini, A., Mathieu, O., Alturaifi, S., Mulvihill, C. R., Petersen, E. L. Laminar flame speed and shock-tube multi-species laser absorption measurements of Dimethyl Carbonate oxidation and pyrolysis near 1 atm. Proc. Comb. Inst., 2021, 38, 977-985.
- [13] Kalitan, D. M., Mertens, J. D., Crofton, M. W., Petersen, E. L. Ignition and oxidation of lean CO/H₂ fuel blends in air. J. propulsion power, 2007, 23, 1291-1301.
- [14] Petersen, E. L., Kalitan, D. M., Barrett, A. B., Reehal, S. C., Mertens, J. D., Beerer, D. J., Hack, R. L., McDonell, V. G. New syngas/air ignition data at lower temperature and elevated pressure and comparison to current kinetics models. Combust. Flame, 149, 2007, 244-247.
- [15] Mittal, G., Sung, C. J., and Yetter, R. A. Autoignition of H₂/CO at elevated pressures in a rapid compression machine. Int. J. Chem. Kinet., 38, 2006, 516-529.
- [16] Herzler, J., Naumann, C. Shock tube study of the ignition of lean CO/H₂ fuel blends at intermediate temperatures and high pressure. Combust. Sci. Technol., 180, 2008, 2015-2028.
- [17] Krejci, M. C., Mathieu, O., Vissotski, A. J., Ravi, S., Sikes, T. G., Petersen, E. L., Kéromnès, A., Metcalfe, W., Curran, H. J. Laminar Flame Speed and Ignition Delay Time Data for the Kinetic Modeling of Hydrogen and Syngas Fuel Blends. J. Eng. Gas Turbines Power, 2013, 135, 021503.
- [18] Thi, L. D., Zhang, Y., Huang, Z. Shock tube study on ignition delay of multi-component syngas mixtures Effect of equivalence ratio. Int. J. Hydrogen Ener. 2014, 39, 6034-6043.
- [19] Lee, H. C., Jiang, L. Y., Mohamad, A. A. A review on the laminar flame speed and ignition delay time of Syngas mixtures. Int. J. Hydrogen Ener., 2014, 39, 1105-1121.
- [20] Fischer, M., Jiang, X. An assessment of chemical kinetics for bio-syngas combustion. Fuel, 2014, 137, 293-305.
- [21] Lee, H. C., Mohamad, A. A., Jiang, L. Y. Comprehensive Comparison of Chemical Kinetics Mechanisms for Syngas/Biogas Mixtures. Energy Fuels 2015, 29, 6126–6145.
- [22] Ouyang, L., Li, H., Sun, S., Wang, X., Lu, X. Auto-ignition of biomass synthesis gas in shock tube at elevated temperature and pressure. Science Bulletin, 2015, 60, 1935-1946.
- [23] Mathieu, O., Kopp, M. M., Petersen E. L. Shock tube study of the ignition of Multi-Component Syngas Mixture with and without Ammonia Impurities. Proceed. Combust. Instit. 2013, 34, 3211-3218.
- [24] Mathieu, O., Hargis, J., Camou, A., Mulvihill, C., Petersen E. L. Ignition delay time measurements behind reflected shock-waves for a representative coal-derived syngas with and without NH3 and H2S impurities. Proceed. Combust. Instit. 2015, 35, 3143-3150.
- [25] Mansfield, A. B., Wooldridge, M. S. The effect of impurities on syngas combustion. Combust. Flame, 2015, 162, 2286-2295.
- [26] Fernandes, Y., Bry, A., de Persis, S. Identification and quantification of gases emitted during abuse tests by overcharge of a commercial Li-ion battery. J. Pow. Sources, 2018, 389, 106-119.
- [27] Ohsaki, T., Kishi, T., Kuboki, T., Takami, N., Shimura, N., Sato, Y., Sekino, M., Satoh, A. Overcharge reaction of lithium-ion batteries. J. Power Sources 2005, 146, 97–100.
- [28] Yuan, Q. Zhao, F., Wang, W., Zhao, Y., Liang, Z., Yan, D. Overcharge failure investigation of lithium-ion batteries. Electrochim. Acta, 2005, 178, 682–688.
- [29] Doughty, D.H., Roth, E.P., Crafts, C.C., Nagasubramanian, G. Henriksen, G., Amine, K. Effects of additives on thermal stability of Li ion cells. J. Power Sources 2005, 146, 116–120.
- [30] Abraham, D., Roth, E., Kostecki, R., McCarthy, K., MacLaren, S., Doughty, D. Diagnostic examination of thermally abused high-power lithium-ion cells. J. Power Sources 2006, 161, 648–657.
- [31] Petersen, E. L.; Rickard, M. J. A.; Crofton, M. W.; Abbey, E. D.; Traum, M. J.; Kalitan, D. M. A facility for gas-and condensed-phase measurements behind shock waves. Meas. Sci. Technol., 2005, 16, 1716-1729.
- [32] Aul, C. J., Metcalfe, W. K., Burke, S. M., Curran, H. J., Petersen, E. L. Ignition and kinetic modeling of methane and ethane fuel blends with oxygen: A design of experiments approach. Combust. Flame, 2013, 160, 1153-1167.
- [33] Pinzon, L. T., Mathieu, O., Mulvihill, C. R., Schoegl, I. M., Petersen, E. L. Ignition Delay Time and H₂O Measurements During Methanol Oxidation Behind Reflected Shock Waves. Comb. Flame, 2019, 203, 143-156.
- [34] Mathieu, O., Pinzon, L. T., Atherley, T. M., Mulvihill, C. R., Schoegl, I. M., Petersen, E. L. Experimental study of ethanol oxidation behind reflected shock waves: Ignition delay time and H₂O laser-absorption measurements. Combust. Flame, 2019, 208 313-326.
- [35] Hong, Z., Davidson, D. F., Hanson, R. K. An improved H₂/O₂ mechanism based on recent shock tube/laser absorption measurements. Combust. Flame, 2011, 154, 633-644.
- [36] Hong, Z., Davidson, D. F., Barbour, E. A., Hanson, R. K. A new shock tube study of the H+ $O_2 \rightarrow OH+ O$ reaction rate using tunable diode laser absorption of H_2O near 2.5 μm . Proc. Comb. Inst., 2011, 33, 1, 309-316.

- [37] Mulvihill, C. R., Petersen, E. L. Concerning shock-tube ignition delay times: an experimental investigation of impurities in the H₂/O₂ system and beyond. Proc. Comb. Inst., 2011, 37, 259-266.
- [38] Baigmohammadi, M., Patel, V., Nagaraja, S., Ramalingam, A., Martinez, S., Panigrahy, S., Mohamed, A., Somers, K. P., Burke, U., Heufer, K. A., Pekalski, A., Curran, H. J. Comprehensive experimental and simulation study of the ignition delay time characteristics of binary blended methane, ethane, and ethylene over a wide range of temperature, pressure, equivalence ratio, and dilution. Energy Fuels, 2020, 34, 8808-8823.
- [39] Alturaifi, S. A., Mulvihill, C. R., Mathieu, O., Petersen, E. L. Speciation measurements in shock tubes for validation of complex chemical kinetics mechanisms: Application to 2-Methyl-2-Butene oxidation. Combust. Flame, 2021, 225, 196-213.
- [40] Morones, A., Turner, M. A., Leon, V. J., Ruehle, K., Petersen, E.L. Validation of a New Turbulent Flame Speed Facility for the Study of Gas Turbine Fuel Blends at Elevated Pressure, Proceedings of ASME Turbo Expo: Power for Land, Sea, and Air. Phoenix, AZ, June 17-21, 2019. https://doi.org/10.1115/GT2019-90394
- [41] Markstein, G. H. Experimental and Theoretical Studies of Flame-Front Stability. J. Aero. Sci., 1951, 18, 199-209.
- [42] Frankel, M. L., Sivashinsky, G. I. On Effects Due to Thermal Expansion and Lewis Number in Spherical Flame Propagation. Combust. Sci. Technol., 1983, 31, 131-138.
- [43] Chen, Z. On the extraction of laminar flame speed and Markstein length from outwardly propagating spherical flames. Combust. Flame, 2011, 158, 291-300.
- [44] Metcalfe, W. K., Burke, S. M., Ahmed, S. S., Curran, H. J. A Hierarchical and Comparative Kinetic Modeling Study of C1–C2 Hydrocarbon and Oxygenated Fuels. Int. J. Chem. Kinet., 2013, 45, 638-675.
- [45] Sikes, T. Mannan, M. S., Petersen, E. L. An experimental study: laminar flame speed sensitivity from spherical flames in stoichiometric CH4–air mixtures. Combust. Sci. Technol., 2018, 190, 1594-1613.
- [46] Lowry, W., de Vries, J., Krejci, M., Petersen, E., Serinyel, Z., Metcalfe, W., Curran, H., G. Bourque, G. Laminar Flame Speed Measurements and Modeling of Pure Alkanes and Alkane Blends at Elevated Pressures. J. Eng. Gas Turbines Power, 2011, 133, 091501.
- [47] Smith, G. P., Golden, D. M., Frenklach, M., Moriarty, N. W., Eiteneer, B., Goldenberg, M., Bowman, C. T., Hanson, R. K., Song, S., Gardiner, W. C., Lissianski, V. V., Qin, Z. (1999), available at: http://combustion.berkeley.edu/gri-mech/version30/text30.html (last accessed 01/27/2022).
- [48] Wang, H., Dames, E., Sirjean, B., Sheen, D. A., Tango, R., Violi, A., Lai, J. Y. W., Egolfopoulos, F. N., Davidson, D. F., Hanson, R. K., Bowman, C. T., Law, C. K., Tsang, W., Cernansky, N. P., Miller, D. L., Lindstedt, R. P. (2010). A high-temperature chemical kinetic model of n-alkane (up to n-dodecane), cyclohexane, and methyl-, ethyl-, n-propyl and n-butyl-cyclohexane oxidation at high temperatures. JetSurF version 2.0, available at:
- http://web.stanford.edu/group/haiwanglab/JetSurF/JetSurF2.0/index.html (last accessed 01/27/2022). [49] Ranzi, E., Cavallotti, C., Cuoci, A., Frassoldati, A., Pelucchi, M., Faravelli, T. New reaction classes in the kinetic
- modeling of low temperature oxidation of n-alkanes. Combust. Flame, 2015, 162, 1679-1691. Available at: http://creckmodeling.chem.polimi.it/menu-kinetics/menu-kinetics-detailed-mechanisms (last accessed 01/27/2022).
- [50] Kéromnès, A., Metcalfe, W. K., Donohoe, N., Das, A. K., Sung, C. J., Herzler, J., Naumann, C., Griebel, P.,
- Mathieu, O., Krejci, M. C., Petersen, E. L., Pitz, W. J., Curran, H. J. An Experimental and Detailed Chemical Kinetic Modelling Study of Hydrogen and Syngas Mixtures at Elevated Pressures. Combust. Flame, 2013, 160, 995-1011. [51] Mathieu, O., Mulvihill, C. R., Petersen, E. L. Assessment of modern detailed kinetics mechanisms to predict CO
- [51] Mathieu, O., Mulvihill, C. R., Petersen, E. L. Assessment of modern detailed kinetics mechanisms to predict CO formation from methane combustion using shock-tube laser-absorption measurements. Fuel, 2019, 236, 1164-1180.



TOC Graphic